Inverse Problems

PAPER • OPEN ACCESS

Tailored interior and boundary parameter transformations for iterative inversion in electrical impedance tomography

To cite this article: Robert Winkler 2019 *Inverse Problems* **35** 114007

OPEN ACCESS
IOP Publishing
Inverse Problems

Inverse Problems **35** (2019) 114007 (22pp)
https://doi.org/10.1088/1361-6420/ab2783

Tailored interior and boundary parameter transformations for iterative inversion in electrical impedance tomography

Robert Winkler

Institute for Applied and Numerical Mathematics, Karlsruhe Institute of Technology, D-76049 Karlsruhe, Germany

E-mail: robert.winkler@posteo.de

Received 29 January 2019, revised 16 April 2019
Accepted for publication 6 June 2019
Published 4 October 2019

Abstract

Electrical impedance tomography is a non-invasive method for imaging the electrical conductivity of an object from electrode measurements on its surface. The underlying mathematical problem is highly nonlinear, severely ill-posed, and several model parameters are usually not known accurately. Despite the strong nonlinearity, iterative Newton-type methods are widely used to tackle the problem numerically.

This work presents and analyzes tailored transformations for the conductivity and for electrode parameters which are favourable in two regards: they remove the constrainedness of the unknown parameters and simultaneously decrease the nonlinearity of the underlying problem. We study the impact of various transformations on the nonlinearity of the problem and demonstrate improved speed of convergence for Newton-type methods while avoiding local minima in the solution space. The presented transformations can conveniently be incorporated into existing iterative solvers as they improve stability and do not require hand-tuned regularization parameters or line-search strategies, thereby bridging a gap between a variety of established conductivity estimation methods and practical applications.

Keywords: electrical impedance tomography, parameter transformation, electrode geometry, nonlinearity, constrainedness, iterative inversion, Newton method

(Some figures may appear in colour only in the online journal)

1. Introduction

1.1. Background

The primary mathematical problem behind electrical impedance tomography (EIT) is the recovery of the spatial *conductivity* distribution inside an object from electrode measurements on its surface, called inverse conductivity problem (ICP). To solve the ICP numerically, the boundary configuration of the measurement setup, i.e. the *surface shape*, the *electrode sizes and positions* and their *contact impedances*, must be known. In contrast to other imaging modalities such as computed tomography or magnetic resonance imaging, the ICP is highly nonlinear, highly sensitive to measurement and modelling errors, and the boundary configuration is not known accurately. As a consequence, methods have been developed to solve an *extended ICP*, that is, to recover the boundary configuration along with the conductivity from the electrode measurements [1–3]. All methods rely on the Fréchet differentiability of the *forward operator* which maps the conductivity and the model parameters to the observed current-to-voltage behaviour at the electrodes.

The forward operator is *nonlinear* in all its input parameters: the current-to-voltage behaviour depends nonlinearly on the conductivity, the electrode contact impedances, their size and position, and the boundary shape. Moreover, all *parameters are bounded* by physical restrictions: the conductivity and the electrode contact impedances are strictly positive, the electrodes have finite positive sizes, and their positions are restricted such that they do not touch or overlap.

1.2. Motivation for using transformations

At first glance, it might not be intuitive to solve the extended ICP with Newton-type methods, which solve parameter problems locally by iterative linearization and may have pitfalls when parameters are constrained. In fact, a wide variety of techniques was developed to avoid high linearization errors, out-of-bounds parameters and oscillatory solutions. These include line-search strategies (e.g. in [2, section 7.2]), 'hand tuning' of regularization parameters for the Tikhonov–Phillips regularization or in the Bayesian framework (e.g. in [4, algorithm 1]), inexact Newton methods [5] or—with more computational effort—cross-validation [6] and L-curve techniques [7].

A popular method for lifting the positivity constraint of the conductivity is to consider the log-conductivity, that is, to apply Newton's method to the logarithm of the conductivity, which is unconstrained. The inverse (exponential) transformation guarantees the positivity of the conductivity after each Newton update. This way, measurement, modelling or linearization errors cannot lead to a violation of the physical model.

Moreover, it was observed that parameter transformations can increase the speed of convergence of Newton-type methods. In the most trivial case of a spatially constant conductivity and in the absence of contact impedances, the electrode measurements are *linear* in the resistivity, the reciprocal of the conductivity. This means that Newton's method converges after one iteration, and there are stable least-squares estimates in case of measurement errors[1] [8, 9]. However, the linearity is violated for non-constant conductivities, and the reciprocal again has a positivity constraint. This sparked the discussion whether conductivity, *log*-conductivity or resistivity should be recovered (e.g. in [10]), and lead to the investigation of conductivity transformations (e.g. in [9, 11, 12]). Recently, theoretical foundations for the

---

[1] This approach is popular to obtain an initial guess for Newton-type methods.

properties of a logarithmic EIT forward operator have been derived, and its advantage in terms of forward accuracy and linearization error for one-step reconstruction has been highlighted numerically, in [13]. Moreover, a transformation of the electrode contact impedances was also considered, while the boundary geometry was assumed to be known.

Moreover, using the Fréchet-differentiability of an extended forward operator with respect to the electrode configuration provides a natural extension for correcting boundary model uncertainties and was studied extensively both regarding theoretical properties [1–3] and in practical applications, where it was found to be superior to other techniques for handling modelling errors [14]. Thus, it is natural to investigate whether applying transformations is also beneficial for recovering boundary model parameters.

The results of this work are focused at (pointwise) conductivity and boundary parameter transformations, but can be conveniently combined with other well-established methods for improving the stability and speed of convergence of the inverse conductivity problem, such as sensitivity-based domain discretizations (investigated theoretically and numerically for various models e.g. in [15–20]), which are not addressed explicitly here.

1.3. Scope and outline

In this work, we pick up and extend the analysis of conductivity transformations from [9]. To that end, we present transformations yielding one-sided ('log-type') and two-sided (sigmoidal) bounds to the conductivity in section 2.6. Then, we investigate the impact of transformations on the nonlinearity for constant and certain non-constant conductivities in sections 3.1 and 3.2 with the help of highly accurate semi-analytic evaluations of the forward operator.

Moreover, we carry over the transformation approach to the boundary parameters in section 2.7 and investigate its impact on the nonlinearity in section 3.3. The result is an unconstrained parameter space for the extended ICP which is favorable for Newton-type methods. It can moreover be used to control the trade-off between conductivity and boundary changes during simultaneous reconstruction, which allows the user to incorporate accuracy assumptions for the boundary configuration. Numerical results for conductivity and boundary parameter transformations within an inexact Newton reconstruction framework are shown in section 4.

In summary, the purpose of this work is to give further insight into the nonlinearity of the ICP and to provide an easy-to-use extension to existing Newton-type methods for EIT applications. MATLAB examples are provided at www.math.kit.edu/ianm3/∼winkler/de.

2. Properties of the complete electrode model

To maintain consistent notation, we briefly restate relevant properties of the ICP and the underlying complete electrode model (CEM). The CEM describes measurements on a finite set of electrodes attached to the object surface and models contact impedances on the electrode-domain-interface. It is generally assumed to be the most realistic among the commonly used electrode models and was verified to reproduce data from tank experiments to measurement precision [21, 22].

2.1. Definition of the complete electrode model

For a compact, simply connected and piecewise smooth Lipschitz domain $\Omega \in \mathbb{R}^n$, $n \in \{2,3\}$, we identify a set of $L \in \mathbb{N}_{\geqslant 2}$ simply connected and pairwise separated electrodes $E_1, \ldots, E_L$ with the subset on $\partial\Omega$ that they cover, that is,

$$\begin{aligned} E_1, \ldots, E_L \subset \partial\Omega \quad & \text{closed and simply connected on } \partial\Omega, \\ E_l \cap E_m = \emptyset \quad & \text{for} \quad l, m \in \{1, \ldots, L\}, l \neq m. \end{aligned}$$

For $n = 2$, we assume w.l.o.g. that the electrodes are ordered consecutively along the boundary. We briefly restate the definition of the CEM in our notation and refer to [23, section 2.1.3.] for a more detailed introduction of the model and its weak formulation using the same notation.

Definition 2.1 (Complete electrode model and measurement operator). Let $\Omega \subset \mathbb{R}^n$ and $E_1, \ldots, E_L \subset \Omega$ as above. Further, denote by $\sigma \in L_+^\infty(\Omega)$ a *conductivity* on Ω and by $z_1, \ldots, z_L \in \mathbb{R}_{>0}$ a set of *contact impedances*. The set of equations

$$-\nabla \cdot (\sigma \nabla u) = 0 \quad \text{on} \quad \Omega, \tag{1}$$

$$f + z_l j_\nu = U_l \quad \text{on} \quad E_l, \qquad l = 1, \ldots, L, \tag{2}$$

$$\int_{E_l} j_\nu \, \mathrm{d}S = I_l, \qquad l = 1, \ldots, L, \tag{3}$$

$$j_\nu = 0 \quad \text{on} \quad \partial\Omega \setminus \{E_1 \cup \ldots \cup E_L\}, \tag{4}$$

where $f = u|_{\partial\Omega}$ and $j_\nu = \nu \cdot \sigma \nabla u$, is called the *CEM*. Herein, ν denotes the boundary normal on $\partial\Omega$. For any *current vector*

$$I = (I_1, \ldots, I_L)^\top \in \mathbb{R}_\diamond^L = \left\{x \in \mathbb{R}^L \colon \sum_{l=1}^{L} x_l = 0\right\},$$

there is a unique $u \in H^1(\Omega)$ and a unique *potential vector* $U = (U_1, \ldots, U_L)^\top \in \mathbb{R}_\diamond^L$ satisfying (1)–(4), and vice versa. The current-to-potential map

$$R_\sigma \in \mathcal{L}(\mathbb{R}_\diamond^L), \quad I \mapsto R_\sigma I = U,$$

is thus well-defined and one-to-one and moreover bounded, linear, and symmetric; see [22]. We call the map

$$F \colon L_+^\infty(\Omega) \supset \mathcal{D}(F) \to \mathcal{L}(\mathbb{R}_\diamond^L), \quad \sigma \mapsto F(\sigma) := R_\sigma = (I \mapsto U),$$

the *forward operator of the CEM*. For $M \in \mathbb{N}$, a *measurement pattern* is defined as

$$\mathcal{I} = \left(I^{(1)} | \ldots | I^{(M)}\right) \in (\mathbb{R}_\diamond^L)^M, \quad \text{where} \quad I^{(m)} \in \mathbb{R}_\diamond^L \text{ for } m = 1, \ldots, M,$$

and its corresponding *measurement data* is defined as

$$\mathcal{U} = (U^{(1)} | \ldots | U^{(M)}) = R_\sigma \mathcal{I} \in (\mathbb{R}_\diamond^L)^M.$$

The operator

$$F_{\mathcal{I}} \colon L_+^\infty(\Omega) \supset \mathcal{D}(F) \to (\mathbb{R}_\diamond^L)^M, \quad \sigma \mapsto F(\sigma)\mathcal{I} = \mathcal{U},$$

is called the *measurement operator* of the CEM. Note that $\operatorname{rank}(\mathcal{I}) = L - 1$ if and only if $I^{(1)}, \ldots, I^{(M)}$ form a frame of $\mathbb{R}_\diamond^L$. A measurement frame of theoretical interest, called $\diamond$*-frame* in this work, consists of $M = L - 1$ (or sometimes $M = L$) current vectors with entries

$$(I_\diamond)_l^{(m)} = \begin{cases} \frac{L-1}{L}, & m = l, \\ -\frac{1}{L}, & \text{otherwise}, \end{cases}$$

for $m, l = 1, \dots, L$, yielding $\mathcal{I}_\diamond^+ = \mathcal{I}_\diamond$ ($^+$ denotes the pseudo-inverse). Thus, $F_{\mathcal{I}_\diamond} = F$.

The ICP in this setting reads

Problem statement 2.2 (Inverse conductivity problem for the complete electrode model). Given a current frame $\mathcal{I}$ and corresponding noisy potential measurements $\mathcal{U}^\delta \in \mathbb{R}^{M\times L}$, find $\sigma \in \mathcal{D}(F)$ satisfying $F(\sigma) \approx \mathcal{U}^\delta$.

2.2. *Differentiability and Newton-type methods for the complete electrode model*

Newton-type methods in EIT rely on the Fréchet differentiability of $F_\mathcal{I}$ [24, 25]. For a single current vector I, the Fréchet derivative of F_I at a conductivity $\sigma \in L^\infty_+(\Omega)$ in direction $\eta \in L^\infty(\Omega)$ is denoted by $F'_\mathcal{I}(\sigma)\eta := U'$, where U' is the unique solution of a weak formulation; see [25, theorem 4.1] and [24]. The standard method for computing the Fréchet derivative is to solve this variational (adjoint state) formulation using the finite element method[2] (FEM). The Fréchet derivative of $F_\mathcal{I}$ is a concatenation of single current vector derivatives and is denoted by

$$F'_\mathcal{I} = \left(F'_{I^{(1)}}, \dots, F'_{I^{(M)}}\right).$$

Given a conductivity estimate $\sigma^{(k)} \in \mathcal{D}(F)$, $k \in \mathbb{N}$, a Newton iteration for the ICP consists of the following steps:

(1) Find a *conductivity update* $\eta^{(k)} \in L^\infty(\Omega)$ such that $\sigma^{(k)} + \eta^{(k)} \in \mathcal{D}(F)$ and $F'_\mathcal{I}(\sigma^{(k)})\eta^{(k)} \approx \mathcal{U}^\delta - F(\sigma^{(k)})$;
(2) Set $\sigma^{(k+1)} = \sigma^{(k)} + \eta^{(k)}$.

Finding an approximate solution in step (1) and choosing a stopping criterion are the main design parameters for Newton-type methods.

2.3. *Recovering boundary parameters*

In practical applications, the boundary parameters of the CEM, i.e. the *contact impedances*, the *electrode positions* and the *boundary shape*, are rarely known accurately. Thus, it can be necessary to recover them *simultaneously with the conductivity* from measured data. For spacial dimension $n = 2$, these four quantities are coupled by conformal equivalence: when allowing non-constant contact impedances, there are distinct settings which have an identical measurement operator.

Conformal equivalence was already used in [26] for Calderón's model on the unit disk and extended to the CEM in [20, 22, 27]. This was used in [20] and [28] to compensate modelling errors by electrode movements, an effect which was further investigated in [29]. For that reason, we *fix the boundary geometry in the scope of this work to avoid under-determination due to conformal equivalence*. However, we want to optimize for the electrode geometry, thus we consider an extension of the classical EIT problem.

---

[2] A MATLAB implementation for the 2D problem is provided by the author under www.math.kit.edu/ianm3/~winkler/. Both 2D and 3D solvers are also available in the EIDORS software at http://eidors3d.sourceforge.net/.

In awareness of a fixed, but possibly inaccurate boundary shape model, we consider the reconstruction result as an approximation to a conformal equivalent of the true, unknown setting. For that reason, we add the individual electrode sizes as an additional degree of freedom since even if they might be known accurately, the sizes of their conformal images are not.

Definition 2.3 (Extended forward operator). We define an *extended forward operator* $\overline{F}$ depending on the conductivity, the electrode locations, sizes and contact impedances by

$$\begin{aligned} \overline{F}\colon \mathcal{D}(F) \times \mathcal{D}_\theta \times \mathcal{D}_{|E|} \times \mathcal{D}_z \quad &\to \quad \mathcal{L}(\mathbb{R}^L_\diamond), \\ \overline{F}\big(\sigma, (\theta_1, \dots, \theta_L), (|E_1|, \dots, |E_L|), (z_1, \dots, z_L)\big) \quad &\mapsto \quad (\mathcal{I} \mapsto \mathcal{U}), \end{aligned}$$

where $(\theta_1, \dots, \theta_L) \in \mathcal{D}_\theta \subset [0, |\partial\Omega|)^L$ parametrizes the center points of each electrode, $(|E_1|, \dots, |E_L|) \in \mathcal{D}_{|E|} \subset [0, |\partial\Omega|)^L$ parametrizes the electrode sizes, and $(z_1, \dots, z_L) \in \mathcal{D}_z \subset \mathbb{R}^L_{>0}$ denote the electrode contact impedances. The corresponding *extended measurement operator* is denoted by

$$\overline{F}_\mathcal{I}\colon \mathcal{D}(\overline{F}) \to (\mathbb{R}^L_\diamond)^M.$$

In [2, theorem 4.1 and corollary 4.2], the Fréchet derivative of the forward operator with respect to an electrode perturbation is given about the origin, that is, at their current shape. In the 2D case, perturbing the electrode boundary simply means to move the end-points of an electrode. Moreover, the integral over the electrode boundary appearing in [2, corollary 4.2] is simply a point-evaluation of the interior potential u at the electrode edges in this case. Since $u|_{\partial\Omega} \in H^{1-\alpha}(\partial\Omega)$ for any $\alpha > 0$, this point evaluation is well-defined.

The explicit formulas in our notation are given in the following for the 2D case. To that end, let

$$E_l = \{\gamma(\theta)\colon -\omega_l \leqslant \theta - \theta_l \leqslant \omega_l\},$$

for an *electrode mid-point* $\theta_l \in [0, |\partial\Omega|)$ and an *electrode half-width* $\omega_l > 0$, $l = 1, \dots, L$, where $\gamma\colon [0, |\partial\Omega|] \to \mathbb{R}^2$ is a continuous, piecewise smooth parametrization of $\partial\Omega$ with $\gamma(0) = \gamma(|\partial\Omega|)$ and $\|\gamma'(\theta)\|_2 = 1$ almost everywhere. To avoid cumbersome notation, we consider the argument θ of γ modulo the length of the boundary $|\partial\Omega|$, where required.

2.4. *Fréchet derivative of the extended operator*

By equally perturbing both electrode edges in the same direction, a *Fréchet derivative with respect to the electrode movement* is given about its current position. For the lth electrode, it is given component-wise (omitting the arguments) by

$$\begin{aligned} \left(\frac{\partial}{\partial\theta_l}\overline{F}\right)_{k,m} &:= \left(\overline{F}'_{\theta_l}\right)_{k,m} \\ &:= -z_l^{-1}\Big[\Big(U_l^{(k)} - u^{(k)}(\gamma(\theta_l + \omega_l))\Big)\Big(U_l^{(m)} - u^{(m)}(\gamma(\theta_l + \omega_l))\Big) \\ &\qquad - \Big(U_l^{(k)} - u^{(k)}(\gamma(\theta_l - \omega_l))\Big)\Big(U_l^{(m)} - u^{(m)}(\gamma(\theta_l - \omega_l))\Big)\Big], \end{aligned}$$

where $\big(u^{(k)}, U^{(k)}\big)$ are the solutions of (1)–(4) for the kth current $I^{(k)}_\diamond$ of the $\diamond$-frame and for conductivity σ. When perturbing both electrode edges by the same amount in opposite direction, a *Fréchet derivative with respect to the electrode size* is given about its current size. For the lth electrode size, it reads

$$\begin{aligned}\left(\frac{\partial}{\partial\,|E_l|}\overline{F}\right)_{k,m} &:= \left(\overline{F}'_{|E_l|}\right)_{k,m}\\ &:= -z_l^{-1}\left[\left(U_l^{(k)}-u^{(k)}(\gamma(\theta_l+\omega_l))\right)\left(U_l^{(m)}-u^{(m)}(\gamma(\theta_l+\omega_l))\right)\right.\\ &\qquad\left.+\left(U_l^{(k)}-u^{(k)}(\gamma(\theta_l-\omega_l))\right)\left(U_l^{(m)}-u^{(m)}(\gamma(\theta_l-\omega_l))\right)\right].\end{aligned}$$

In particular, $\overline{F}'_{\theta_l}$ and $\overline{F}'_{|E_l|}$ only differ by one sign in the sum.

The Fréchet derivative of the forward operator with respect to the contact impedance z_l of the lth electrode, studied e.g. in [3], is given by

$$\left(\frac{\partial}{\partial z_l}\overline{F}\right)_{k,m} := \left(\overline{F}'_{z_l}\right)_{k,m} = -\frac{1}{z_l^2}\int_{E_l}\left(U_l^{(k)}-u^{(k)}\right)\left(U_l^{(m)}-u^{(m)}\right)\,\mathrm{d}S,$$

where $(u^{(k)},U^{(k)})$ is the solution of (1)–(4) for the current vector $I_\diamond^{(k)}$. The integral can be approximated e.g. with a quadrature rule on the point values of FEM approximations of $u^{(k)}$ and $u^{(m)}$, $k,m=1,\ldots,L$.

The Fréchet derivative for an extended measurement operator with arbitrary measurement pattern $\mathcal{I}$ can be obtained by a multiplication with the particular currents, i.e.

$$\begin{aligned}\left(\overline{F}'_{\mathcal{I},\theta_l}\right)_{k,m} &= \left(\overline{F}'_{\theta_l}I^{(m)}\right)_k,\\ \left(\overline{F}'_{\mathcal{I},|E_l|}\right)_{k,m} &= \left(\overline{F}'_{|E_l|}I^{(m)}\right)_k \quad\text{and}\\ \left(\overline{F}'_{\mathcal{I},z_l}\right)_{k,m} &= \left(\overline{F}'_{z_l}I^{(m)}\right)_k\end{aligned}$$

for $k,l=1,\ldots,L$ and $m=1,\ldots,M$, respectively, where again $\mathcal{I}=\left\{I^{(1)},\ldots,I^{(M)}\right\}$.

2.5. Newton's method for the extended inverse conductivity problem

A Newton iteration for the extended ICP can be defined analogous to the classical ICP. Denote by $\sigma^{(k)}$ the conductivity estimate after the kth Newton iteration and further by

$$\begin{aligned}\boldsymbol{z}^{(k)} &= (z_1^{(k)},\ldots,z_L^{(k)}),\\ \boldsymbol{\theta}^{(k)} &= (\theta_1^{(k)},\ldots\theta_L^{(k)}) \quad\text{and}\\ \boldsymbol{\omega}^{(k)} &= (\omega_1^{(k)},\ldots,\omega_L^{(k)})\end{aligned}$$

the contact impedance estimates and electrode configuration estimate after the kth iteration. The task of Newton's method for the extended ICP in the $k+1$th iteration is to find a Newton update

$$\boldsymbol{\Delta}^{(k)} = \left(\eta^{(k)},\boldsymbol{\Delta z}^{(k)},\boldsymbol{\Delta\theta}^{(k)},\boldsymbol{\Delta\omega}^{(k)}\right) \in L^\infty(\Omega)\times\mathbb{R}^L\times\mathbb{R}^L\times\mathbb{R}^L$$

satisfying

$$F'_{\mathcal{I}}(\sigma^{(k)};\boldsymbol{z}_L^{(k)};E_1^{(k)},\ldots,E_L^{(k)})[\boldsymbol{\Delta}^{(k)}] \approx \mathcal{U}^\delta - F_{\mathcal{I}}(\sigma^{(k)};\boldsymbol{z}^{(k)};E_1^{(k)},\ldots,E_L^{(k)})$$

such that

$$\sigma^{(k)}+\eta^{(k)}\in\mathcal{D}(F), \tag{5}$$

Table 1. Definition, inverse transformation and range of various conductivity transformations.

Transformation t_*	Inverse $t_*^{-1}(\sigma_*)$	Domain and range
$t_{\mathrm{Id}}(\sigma) := \sigma$	σ_*	$t_{\mathrm{Id}}\left((0,\infty)\right) = (0,\infty)$
$t_{\log}(\sigma) := -\log(\sigma)$	$e^{-\sigma_*}$	$t_{\log}\left((0,\infty)\right) = (\infty,-\infty)$
$t_\rho(\sigma) := \sigma^{-1}$	σ_*^{-1}	$t_\rho\left((0,\infty)\right) = (\infty,0)$
$t_{\sigma\rho}(\sigma) := \frac{3-\sigma^2}{4\sigma}$	$\sqrt{3+4\sigma_*^2} - 2\sigma_*$	$t_{\sigma\rho}\left((0,\infty)\right) = (\infty,-\infty)$
$t_{\mathrm{tl}}(\sigma) :=$ $\tan\left(\frac{\pi(\log(\sigma)-\log(c_{\min}))}{\log(c_{\max})-\log(c_{\min})} - \frac{\pi}{2}\right)$	$\exp\left[\log(c_{\min}) + (\log(c_{\max}) - \log(c_{\min})) \cdot \pi^{-1}\left(\tan^{-1}(\sigma_*) + \frac{\pi}{2}\right)\right]$	$t_{\mathrm{tl}}\left((c_{\min}, c_{\max})\right) = (-\infty,\infty)$

$$z^{(k)} + \boldsymbol{\Delta} z^{(k)} \geqslant 0, \tag{6}$$

and such that $E_1^{(k+1)}, \ldots, E_L^{(k+1)}$ is an admissible electrode configuration, where

$$E_l^{(k+1)} = \left\{\gamma(\theta)\colon\; -(\omega_l^{(k)} + \Delta\omega_l^{(k)}) \leqslant \theta - (\theta_l^{(k)} + \Delta\theta_l^{(k)}) \leqslant (\omega_l^{(k)} + \Delta\omega_l^{(k)})\right\}. \tag{7}$$

2.6. Transformed forward operator

Instead of linearizing the measurement operator directly, we want to apply the Newton step to a transformation of the conductivity coefficient. To that end, we consider injective C^1-transformations

$$t_*\colon (0,\infty) \to \mathbb{R}, \quad \sigma \mapsto t_*(\sigma) =: \sigma_*.$$

Assuming, for simplicity, that the conductivity can be evaluated pointwise, we consider a *transformed forward operator* F_* defined as

$$F_*(t_*(\sigma)) = F(\sigma), \quad \text{that is,} \quad F_*(\sigma_*) = F(t_*^{-1}(\sigma_*)), \tag{8}$$

where t_* operates pointwise on σ, i.e. $\sigma_*(x) = t_*(\sigma(x))$ for $x \in \Omega$. This extends straightforward to general $\sigma \in L_+^\infty(\Omega)$. The transformed measurement operator $(F_*)_{\mathcal{I}}$ is defined analogously.

Table 1 displays the *identity transformation* t_{Id}, the *negative log-conductivity* $t_{\log}$, the *resistivity transformation* (reciprocal conductivity) t_ρ, the *σ-ρ-transformation* $t_{\sigma\rho}$ as well as the $\tan$-log-*transformation* t_{tl}. The latter transformation is special since its domain enforces the conductivity to be strictly bounded from two sides, $0 < c_{\min} \leqslant \sigma \leqslant c_{\max} < \infty$. The σ-ρ-transformation is a convex combination of the negative conductivity and the resistivity, namely $\alpha(-\sigma) + (1-\alpha)\sigma^{-1}$ for $\alpha = \frac{1}{4}$. As the sum of two strictly decreasing functions, it is one-to-one. The choice of α satisfies a certain optimality condition, although the exact value is uncritical. Moreover, this transformation has the asymptotic of the identity for $\sigma \to \infty$ and the asymptotic of the resistivity for $\sigma \to 0$. For details, see [23, section 4.2].

2.7. Transformed extended forward operator

Similarly to the conductivity constraints, we have restrictions for the electrode geometry: all electrodes have positive size, do not change order, and do not overlap. To implicitly enforce

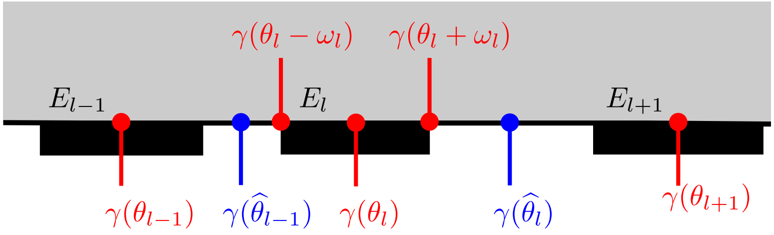

Figure 1. Parametrization of the electrodes on the boundary. The gap centers $\gamma(\widehat{\theta}_1), \ldots, \gamma(\widehat{\theta}_L)$ will act as barriers for the electrode movement and deformation in each Newton iteration.

these conditions when applying Newton type updates, we again consider transformations from bounded to unbounded parameter spaces. We want to perform electrode changes independently of the neighboring electrodes, thus we introduce per-iteration *barriers* at the electrode gap centers. The gap centers are parametrized by

$$\widehat{\theta}_l := \frac{1}{2}\left[(\theta_{l+1} - \omega_{l+1}) - (\theta_l + \omega_l)\right].$$

This situation is depicted in figure 1, where the electrode center and their parameters θ_l are depicted in red, while the gap centers and their parameters $\widehat{\theta}_l$ are depicted in blue.

Now we allow each electrode E_l, $l = 1, \ldots, L$, to move and change size within the boundary section

$$\left\{\gamma(\theta) \colon \widehat{\theta}_{l-1} < \theta < \widehat{\theta}_l\right\},$$

i.e. we want the updated parameters $\theta_l^{(k+1)}$ and $\omega_l^{(k+1)}$ to satisfy

$$\widehat{\theta}_{l-1}^{(k)} < \theta_l^{(k+1)} - \omega_l^{(k+1)} < \theta_l^{(k+1)} + \omega_l^{(k+1)} < \widehat{\theta}_l^{(k)} \quad (\text{modulo } |\partial\Omega|), \quad l = 1, \ldots, L,$$

after the kth Newton step. This is a coupled restriction for each electrode size and position. To decouple the conditions, we further split this available space into one part for the electrode movement and another part for the electrode size change, as shown in figure 2. Therein, the yellow sections of the boundary depict the parts of the boundary 'reserved' for the electrode resizing, and the green sections depict the parts for the electrode movement.

For the electrode sizes and the parameters of the locations, we thus obtain restrictions from below and from above. One possibility to handle this restriction is to use a sigmoidal transformation for the parameters, mapping the interval boundaries to $\pm\infty$. First, we introduce a lower bound $\zeta_l^{(k)}$ satisfying

$$0 < \zeta_l^{(k)} < \omega_l^{(k+1)}$$

for the updated half-width $w_l^{(k+1)}$ of the lth electrode after the kth iteration to ensure numerical stability for the FEM forward solutions[3]. In our numerical examples, $\zeta_l^{(k)} := \frac{2}{3}\omega_l^{(k)}$ is used. Moreover, define

---

[3] The forward model might get unstable when electrodes or gaps shrink to a point.

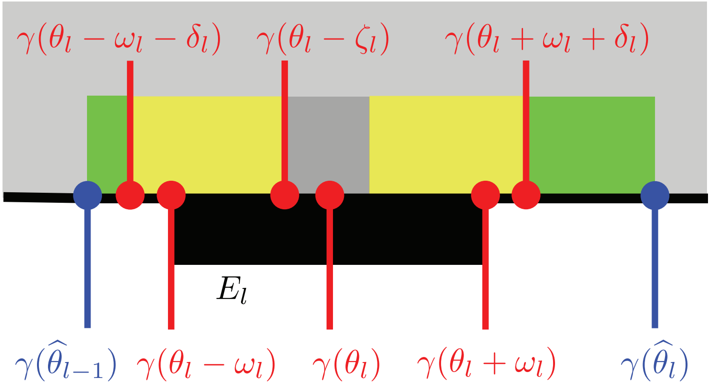

Figure 2. Green: reserved for electrode movement. Yellow: reserved for electrode resizing. Dark gray: preserved minimum electrode width in the *k*th iteration.

$$\begin{aligned}
\delta_l &:= \frac{1}{2}\min\left\{\widehat{\theta}_l - (\theta_l + \omega_l), (\theta_l - \omega_l) - \widehat{\theta}_{l-1}\right\} > 0, && \text{(electrode growth bound)}\\
\overline{\delta}_l &:= \widehat{\theta}_l - \theta_l - \omega_l - \delta_l > 0, \quad \text{and} && \text{(right movement bound)}\\
\underline{\delta}_l &:= \theta_l - \widehat{\theta}_{l-1} - \omega_l - \delta_l > 0, && \text{(left movement bound)},
\end{aligned}$$

for each $l = 1, \ldots, L$, all possibly modulo $|\partial\Omega|$. Using these quantities, we restrict the electrode movement in the *k*th Newton step to

$$-\underline{\delta}_l^{(k)} + \theta_l^{(k)} < \theta_l^{(k+1)} < \overline{\delta}_l^{(k)} + \theta_l^{(k)} \tag{9}$$

and the electrode resizing to

$$\zeta_l^{(k)} < \omega_l^{(k+1)} < \omega_l^{(k)} + \delta_l^{(k)}. \tag{10}$$

In figure 2, introduced quantities simply parametrize the boundaries of the yellow and green sections for the electrode resizing and movement, respectively.

One possibility for defining a sigmoidal transformation is to choose again the tangent, i.e.

$$t_{\theta_l,\tan}^{(k)}(\theta) = \tan\left(\frac{\pi}{\overline{\delta}_l^{(k)} + \underline{\delta}_l^{(k)}}\left(\theta + \underline{\delta}_l^{(k)} - \theta_l^{(k)} - \frac{\pi}{2}\right)\right)$$

for the position update and

$$t_{\omega_l,\tan}^{(k)}(\omega) = \tan\left(\frac{\pi}{\omega_l^{(k)} + \delta_l^{(k)} - \zeta_l^{(k)}}\left(\omega - \zeta_l^{(k)}\right) - \frac{\pi}{2}\right)$$

for size update of the *l*th electrode in the *k*th iteration, respectively. These transformations map the admissible interval for the position and size updates to the real line.

3. Nonlinearity of the forward operator

The nonlinearity of the ICP for non-constant conducitivities is obvious: for example, when $\sigma_{\chi_B} \to \infty$ on a subset $B \subset \Omega$ of the domain with positive distance to the boundary, we still obtain a finite Neumann–Dirichlet problem in the limit case, and thus $\|F\| \not\to \infty$.

We next demonstrate the impact of several conductivity transformations on the nonlinearity of F. To that end, we generate highly accurate references using semi-analytic solutions of the CEM on a circular domain with

(a) a homogeneous conductivity,
(b) (possibly non-centered) circular inhomogeneities,

as introduced in [20]. We choose a generic electrode setup with $L = 16$ equally distributed electrodes with $|E|_l = \frac{2\pi}{32}$, $l = 1, \ldots, L$, and $z = 10^{-4}$, on the unit disk $\Omega = B_1(\mathcal{O})$. On this domain we define, for any $\xi > 0$,

$$\sigma_\xi(x) := \xi, \quad x \in \Omega, \tag{11}$$

for the homogeneous conductivity case (a) and

$$\sigma_\xi(x) := \begin{cases} 1, & x \in \Omega \setminus B, \\ \xi, & x \in B, \end{cases} \tag{12}$$

for some circular inclusion $B \subset \Omega$ for case (b). Then, we study the behaviour of $\|F(\sigma_\xi) - F(\sigma_1)\|_{\mathrm{Fro}}$ as well as the *conductivity nonlinearity indicator*

$$\kappa_{\mathrm{cond}}(\xi, t_*) := \frac{\|F(\sigma_\xi) - F(\sigma_1)\|_{\mathrm{Fro}}}{\|t_*(\sigma_\xi) - t_*(\sigma_1)\|_\infty}$$

for various (pointwise) conductivity transformations $t_* \colon (0, \infty) \to \mathbb{R}$. If F is linear in the transformed conductivity t_*, then κ_{cond} is constant in ξ (the converse is not necessarily true). In that sense, the variation of κ_{cond} in ξ is an indicator for the nonlinearity of F in the transformed conductivity.

3.1. Nonlinearity for homogeneous conductivities

For vanishing contact impedance and homogeneous conductivity, the forward operator is linear in the resistivity. Thus for small contact impedances $z \ll \frac{1}{\|\sigma_\xi\|_\infty}$, we expect the forward operator to be almost linear. Figure 3(a) shows the behaviour of the nonlinearity indicator $\kappa_{\mathrm{cond}}(\xi, t_*)$ versus the parameter ξ for the conductivity transformations t_{Id}, t_ρ, $t_{\log}$ and $t_{\sigma\rho}$. A non-constant line indicates nonlinearity of the forward operator with respect to the transformed conductivity parameter. We observe how the σ-ρ-transform $t_{\sigma\rho}$ behaves similar to the resistivity transform t_ρ for small conductivities and similar to the identity t_{Id} for large conductivities. The forward operator is almost linear in the resistivity, whereas the log-transform and the σ-ρ-transform give a good trade-off between nonlinearity and unconstrainedness.

3.2. Nonlinearity for inhomogeneous conductivities

Figures 3(b)–(d) show the behaviour of the nonlinearity indicator $\kappa_{\mathrm{cond}}(\xi, t_*)$ versus the parameter ξ for the conductivity transformations t_{Id}, t_ρ, $t_{\log}$ and $t_{\sigma\rho}$ for conductivities with circular inhomogeneities of decreasing radius, i.e. (b) $B = B_{0.8}(\mathcal{O})$, (c) $B = B_{0.5}(\mathcal{O})$ and (d) $B = B_{0.2}(\mathcal{O})$, respectively. At high contrast ($\xi \ll 1$ or $\xi \gg 1$), for decreasing size of the inhomogeneity, the nonlinearity for the log-transform decreases, while the nonlinearity for the σ-ρ-transform increases.

This suggests that the log-transform might be better suited for recovering small, high-contrast inclusions inside a homogeneous medium, while the σ-ρ-transform might be better suited for recovering large inhomogeneities with lower contrast.

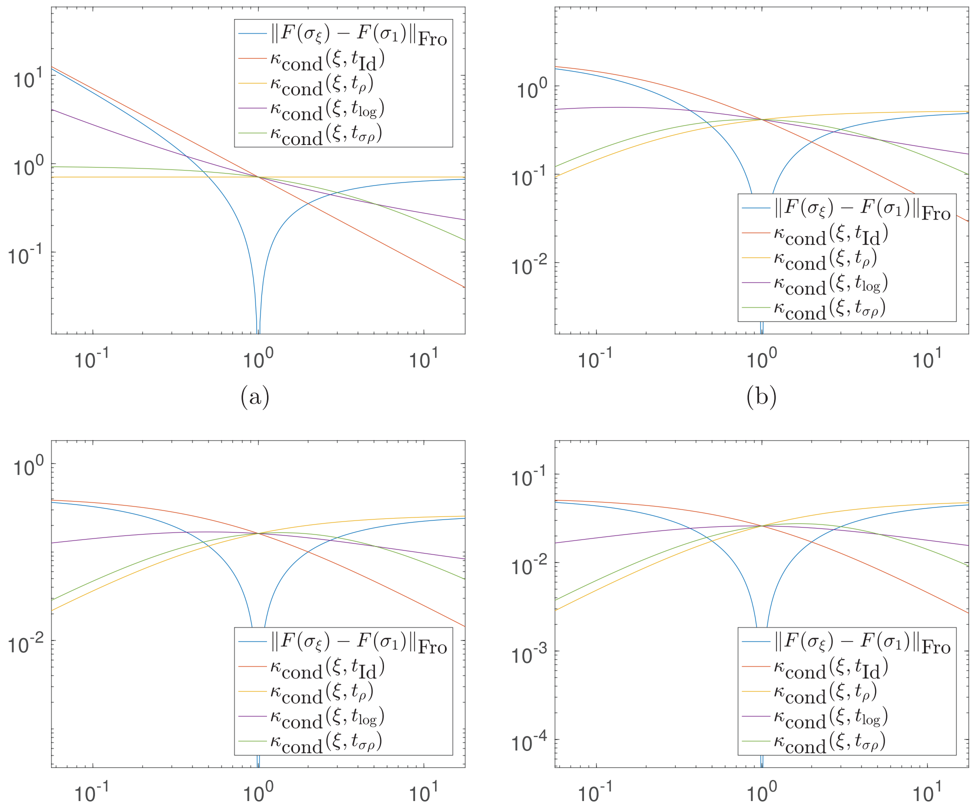

(a) (b)

(c) (d)

Figure 3. (a) Nonlinearity indicator κ_{cond} versus conductivity parameter ξ for homogeneous conductivities, defined in (11). The forward operator is almost linear in the resistivity, which can be seen from the almost constant nonlinearity indicator $\kappa_{\mathrm{cond}}(\xi, t_\rho)$. The σ-ρ-transform behaves similar to the resistivity for small conductivities and similar to the identity for large conductivities. (b)–(d) As in (a), but with ξ being a conductivity with a centered circular inhomogeneity, as defined in (12). At high contrast, for decreasing size of the inhomogeneity, the nonlinearity for the log-transform decreases, while the nonlinearity for the σ-ρ-transform increases. Note the scale difference in (b)–(d). (b) Inhomogeneity with radius 0.8. (c) Inhomogeneity with radius 0.5. (d) Inhomogeneity with radius 0.2.

3.3. Nonlinearity of the extended forward operator

In section 2.7, we introduced parameter transformations also for the extended problem, i.e. for recovering the electrode shapes, sizes, and contact impedances. Analogously to the conductivity nonlinearity indicator, we introduce *indicators for the nonlinearity* with respect to the *electrode positions* as

$$\kappa_{\mathrm{pos}}(p, t_{\theta,*}) = \frac{\|\overline{F}(\ldots, (\theta_1 + p_1, \ldots, \theta_L + p_L), \ldots) - \overline{F}(\ldots, (\theta_1, \ldots, \theta_L), \ldots)\|_{\mathrm{Fro}}}{\sum_{l=1}^{L} |t_{\theta_l,*}(\theta_l + p_l) - t_{\theta_l,*}(\theta_l)|}, \quad p = (p_1, \ldots, p_L) \in \mathbb{R}^L,$$

with respect to the *electrode sizes* as

$$\kappa_{\text{size}}(s, t_{\omega,*}) = \frac{\left\|\overline{F}(\ldots,(\omega_1+s_1,\ldots,\omega_L+s_L),\ldots) - \overline{F}(\ldots,(\omega_1,\ldots,\omega_L),\ldots)\right\|_{\text{Fro}}}{\sum_{l=1}^{L} |t_{\omega_l,*}(\omega_l+s_l) - t_{\omega_l,*}(\omega_l)|}, \quad s=(s_1,\ldots,s_L)\in\mathbb{R}^L,$$

and with respect to the *contact impedances* as

$$\kappa_{\text{contact}}(c, t_{z,*}) = \frac{\left\|\overline{F}(\ldots,z_1+c_1,\ldots,z_L+c_L) - \overline{F}(\ldots,z_1,\ldots,z_L)\right\|_{\text{Fro}}}{\sum_{l=1}^{L} |t_{z_l,*}(z_l+c_l) - t_{z_l,*}(z_l)|}, \quad c=(c_1,\ldots,c_L)\in\mathbb{R}^L,$$

respetively.

Using the same 16 electrode setup as before, we evaluate κ_{pos} using again semi-analytic solutions and letting

$$p = (p_1, 0, \ldots 0) \quad \text{for} \quad p_1 \in \left(-\frac{2\pi}{32\cdot 1.05}, +\frac{2\pi}{32\cdot 1.05}\right) \tag{13}$$

(to avoid electrode gaps going to zero). The scaling parameters in the tangent-transform are set as $\underline{\delta}_1 = \overline{\delta}_1 = \frac{2\pi}{32}$. The result is shown in figure 4(a). We observe an increase of the nonlinearity indicator when the electrode approaches its left or right neighbor in the untransformed case, indicating that linearization might over-estimate electrode location changes and lead to invalid (overlapping) electrode configurations. This effect is compensated when using the tangent transform, which by design prevents illegal electrode configurations.

Similarly, we use

$$s = (s_1, 0, \ldots, 0) \quad \text{for} \quad s_1 \in \left(-\frac{2\pi}{64\cdot 1.05}, +\frac{2\pi}{32\cdot 1.05}\right) \tag{14}$$

to perturb the size of the first electrode for the same 16 electrode setup. The resulting nonlinearity indicators $\kappa_{\text{size}}(s, t_{\omega,\text{Id}})$ and $\kappa_{\text{size}}(s, t_{\omega,\tan})$ are shown in figure 4(b). The nonlinearity increases as the electrode size tends to zero, indicating that linearization may lead to an underestimation and even negative electrode sizes in the untransformed case. Again, the damping effect of the tangent transform prevents this.

Finally, consider varing contact impedances with a base value of $z = 1$ and contact impedance deltas (on a logarithmic scale) of

$$c = (c_1, c_1, \ldots, c_1) \quad \text{for} \quad c_1 \in (10^{-3} - 1,\ 10^{+3} - 1). \tag{15}$$

The resulting nonlinearity indicators $\kappa_{\text{contact}}(c, t_{z,\text{Id}})$, $\kappa_{\text{contact}}(c, t_{z,\sigma\rho})$ and $\kappa_{\text{contact}}(c, t_{z,\log})$ are shown in figure 4(c). The identity transform does not resolve the constrainedness of the contact impedance, but $\kappa_{\text{contact}}(c, t_{z,\text{Id}})$ indicates that it is almost linear in this setting. In contrast, the log-transform resolves constrainedness, but higher nonlinearity is indicated by $\kappa_{\text{contact}}(c, t_{z,\log})$. The $\sigma\rho$-transform resolves constrainedness and $\kappa_{\text{contact}}(c, t_{z,\sigma\rho})$ indicates that it also keeps the nonlinearity limited in this setting. In particular, the indicator is almost constant for very high contact impedances, which may occur e.g. when electrodes are badly attached.

4. Numerical evaluations

The conductivity and boundary parameter transformations introduced in sections 2 and 3 can be incorporated into any solver making use of the linearization of the forward operator. The numerical evaluations here use the well-established CG-REGINN [30] applied to

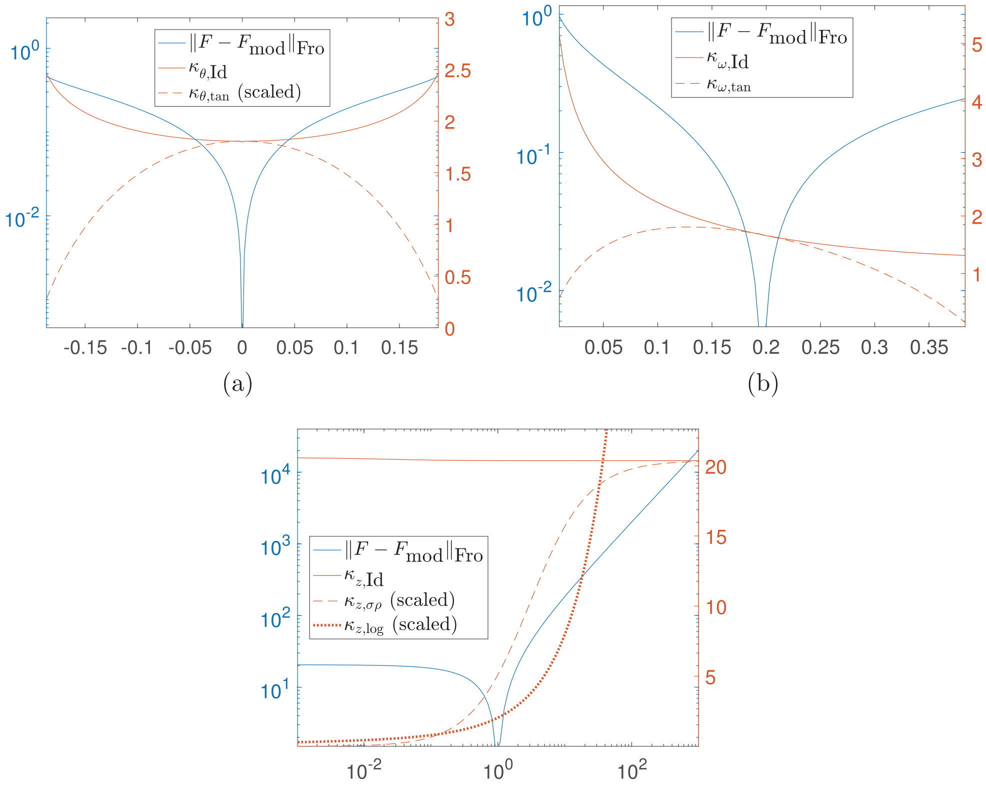

(a) (b)

(c)

Figure 4. (a) Nonlinearity indicator κ_{pos} versus electrode location perturbation p as defined in (13). For the untransformed conductivity, the nonlinearity increases as the electrode approaches the neighboring electrodes. (b) Nonlinearity indicator κ_{size} versus electrode size change s as defined in (14). As the electrode size decreases, the nonlinearity indicator in the untransformed case increases as well, suggesting that electrode size changes are over-estimated during linearization. (c) Nonlinearity indicator $\kappa_{\mathrm{contact}}$ versus contact impedance $z + c$ as defined in (15). The log and $\sigma\rho$ transformation have similar damping behaviour near vanishing contact impedances, but the $\sigma\rho$ transformation behaves similar to the untransformed case for high contact impedances.

the ICP for the CEM [25], using the initializations, error model, sensitivity-based weighting scheme and stopping criterion as presented in [9], called model-aware Newton-type Inversion scheme (MANTIS). In particular, MANTIS estimates an initial constant conductivity and corresponding electrode contact impedances based on an optimality condition, and moreover provides an estimate for the measurement noise level. Details for the assembly of the extended system equations in this setting are beyond the scope of this work and can be found in [23].

After introducing the considered setting in section 4.1, we will present EIT reconstructions of the MANTIS algorithm using the extended forward operator and the introduced transformations for a configuration simulating badly attached electrodes (section 4.3), highly fluctuating contact impedances (section 4.4), wrong boundary geometry (section 4.5) and the combination of fluctuating contact impedances and wrong boundary geometry (section 4.6).

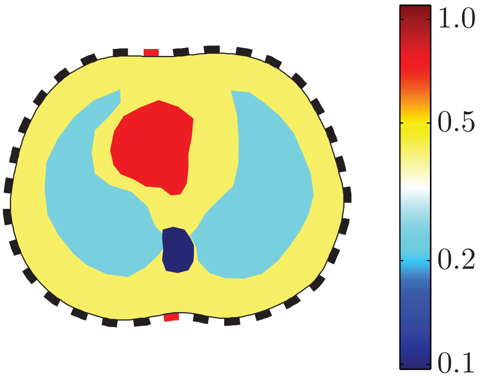

Figure 5. 2D setting resembling a human thorax cross section.

For reference, we will also show the the reconstruction results when no corrections for boundary parameters are estimated at all, i.e. when the extended forward operator is not used.

The number of Newton steps $k_* \in \mathbb{N}$ is a practical indicator for the nonlinearity of an inverse problem: (unregularized) linear problems converge after a single iteration. The value is given, along with the relative reconstruction error $e_{\mathrm{rel}} \geqslant 0$, for each reconstruction, see [23, chapter 4.4.5. and equation (6.1)] for definitions and further background.

4.1. Setting

The setting considered in this section is a 2D domain resembling the cross section of a human thorax with a highly conductive inclusion ('heart', $\sigma = 0.75$), two resistive inclusions ('lungs', $\sigma = 0.24$), and one highly resistive inclusion ('spine', $\sigma = 0.05$) in an otherwise homogeneous background ('soft tissue', $\sigma = 0.42$). The conductivity values are chosen to agree with those of the experimental setup [31]. The domain Ω is scaled to fit into the square $[-1,1]^2$, resulting in a total circumference of $|\partial\Omega| \approx 7.377$. We assume to have a boundary model with $L = 32$ electrodes equi-spaced electrodes covering 50% of the surface. This is depicted in figure 5. The contact impedances are $z_1, \ldots, z_L = 0.05$ unless stated otherwise.

Measurement data for this setting is simulated using the same FEM forward solver, but on a much finer mesh, which is *not* a refinement of the mesh used for reconstruction, to minimize inverse crime. Noise is added according to the noise model of [23, chapter 2.2.2.] with a relative noise level of $\delta^{\mathrm{rel}} = 0.1\%$.

4.2. Reconstructions for perfectly known boundary parameters

For reference, we first show the reconstruction for perfectly modelled boundary geometry and the conductivity transformations t_{Id} and $t_{\log}$ in figure 6. The result for $t_{\sigma\rho}$ is visually indistinguishable from $t_{\log}$ and converges with $k_* = 16$ and $e_{\mathrm{rel}} = 14.94\%$.

4.3. Badly attached electrodes

Now we consider a setting with with two electrodes in the non-convex part of the boundary (marked red in figure 5) having a high contact impedance:

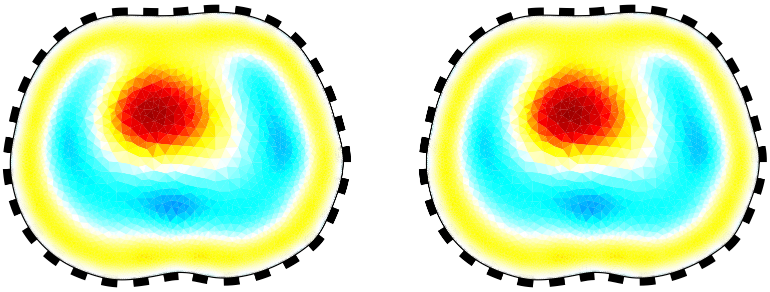

(a) Using F, t_{Id}: $k_* = 19, e_{\mathrm{rel}} = 15.00\%$.

(b) Using F, $t_{\log}$: $k_* = 18, e_{\mathrm{rel}} = 14.97\%$.

Figure 6. Reconstructions for the MANTIS algorithm to F and using exact boundary parameters. (a) Using F, t_{Id}: $k_* = 19, e_{\mathrm{rel}} = 15.00\%$. (b) Using F, $t_{\log}$: $k_* = 18, e_{\mathrm{rel}} = 14.97\%$.

$$z_l = \begin{cases} 1, & l \in \{10, 25\}, \\ 0.05, & l \in \{1, \dots, 32\} \setminus \{10, 25\}. \end{cases}$$

In practice, this can happen e.g. when the electrodes are badly attached. Results without and with simultaneous reconstruction of conductivity and contact impedances are shown in figure 7. Not accounting for varying contact impedances (MANTIS initialized them with $z_1, \dots, z_L = 0.082$) yields highly oscillating interior conductivities shown in figures 7(a) and (d) for conductivity transformations t_{Id} and $t_{\log}$, respectively. They correspond to local minima of the ICP. Recovering the contact impedances simultaneously (using $t_{z,\log}$ or $t_{z,\tan}$) removes these oscillations, tremendously improves the conductivity reconstruction and improves speed of convergence (figures 7(b), (c), (e) and (f)). For reference, using $t_{\sigma\rho}$ as conductivity transformation yields $k_* = 48$, $e_{\mathrm{rel}} = 42.97\%$ with fixed contact impedances and $k_* = 28$, $e_{\mathrm{rel}} = 14.52\%$ when using the $t_{z,\tan}$ for the contact impedances.

We observe that best results are achieved when using the $t_{\log}$ as a conductivity transformation and $t_{z,\tan}$ with limits $[10^{-4}, 10^{+4}]$ as a contact impedance transformation. The contact impedances are recovered accurately; see figure 8.

4.4. Fluctuating contact impedances

This setting is similar to section 4.3, but now all contact impedances are randomly chosen:

$$z_l \in [10^{-3}, 0.2], \quad l = 1, \dots, 32.$$

The reconstructions are shown, analogously to section 4.3, in figure 9. The true and estimated contact impedances are shown in figure 10.

Again, best performance is achieved using $t_{\log}$ as conductivity transformation and $t_{z,\tan}$ as contact impedance transformation. Using conductivity transformation $t_{\sigma\rho}$ yields almost identical performance and is therefore omitted here.

4.5. Wrong boundary geometry

Now, we assume that the exact boundary geometry of the setting is unknown for reconstruction and perform the estimation on an elliptically shaped domain. When estimating the electrode sizes and positions using the extended forward operator, as described in section 2.3, we

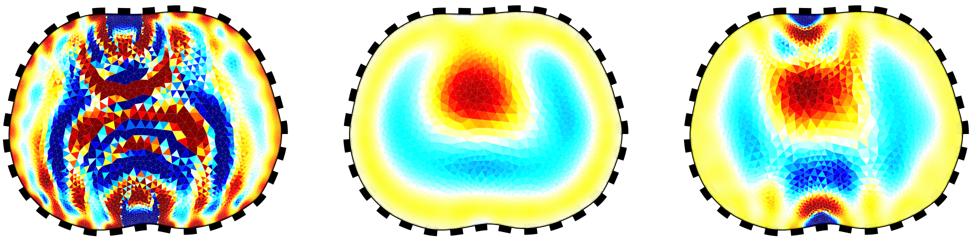

(a) Using F, t_{Id}: $k_* = 87, e_{\mathrm{rel}} = 80.77\%$.

(b) $\overline{F}$, t_{Id}, $t_{z,\log}$: $k_* = 29, e_{\mathrm{rel}} = 14.12\%$.

(c) $\overline{F}$, t_{Id}, $t_{z,\tan}$: $k_* = 19, e_{\mathrm{rel}} = 18.86\%$.

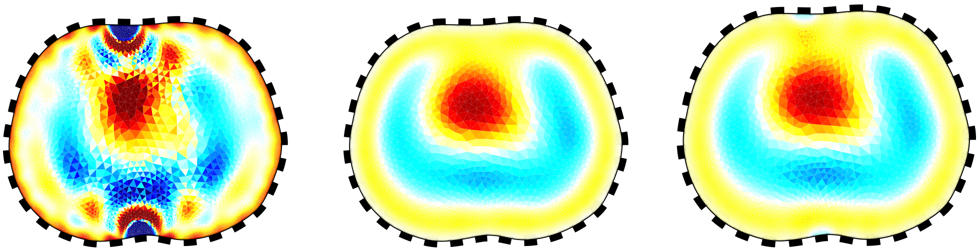

(d) F, $t_{\log}$: $k_* = 26, e_{\mathrm{rel}} = 28.42\%$.

(e) $\overline{F}$, $t_{\log}$, $t_{z,\log}$: $k_* = 36, e_{\mathrm{rel}} = 14.55\%$.

(f) $\overline{F}$, $t_{\log}$, $t_{z,\tan}$: $k_* = 21, e_{\mathrm{rel}} = 14.07\%$.

Figure 7. Reconstructions in the presence of two unknown high contact impedances. Contact impedances are *not* estimated in (a) and (d) and estimated using a logarithmic parameter transformation ((b) and (e)) or a tangential transformation with limits $[10^{-4}, 10+4]$ ((c) and (f)). Top row: conductivity is recovered directly. Bottom row: conductivity is recovered using $t_{\log}$. (a) Using F, t_{Id}: $k_* = 87, e_{\mathrm{rel}} = 80.77\%$. (b) $\overline{F}$, t_{Id}, $t_{z,\log}$: $k_* = 29, e_{\mathrm{rel}} = 14.12\%$. (c) $\overline{F}$, t_{Id}, $t_{z,\tan}$: $k_* = 19, e_{\mathrm{rel}} = 18.86\%$. (d) F, $t_{\log}$: $k_* = 26, e_{\mathrm{rel}} = 28.42\%$. (e) $\overline{F}$, $t_{\log}$, $t_{z,\log}$: $k_* = 36, e_{\mathrm{rel}} = 14.55\%$. (f) $\overline{F}$, $t_{\log}$, $t_{z,\tan}$: $k_* = 21, e_{\mathrm{rel}} = 14.07\%$.

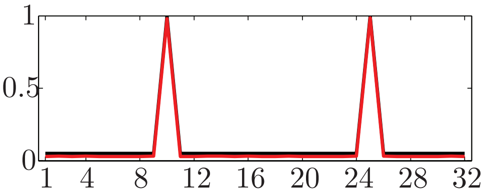

Figure 8. Exact (black) and recovered (red) contact impedances at the 32 electrodes the of setting considered in section 4.3.

allow the estimator to converge towards a solution which is conformally equivalent to the true geometry. The computed relative error of the solution is measured versus a conformal equivalent of the thorax shaped setting on the ellipse. It was obtained using the Schwarz–Christoffel toolbox (version 2.3) provided by Tobin Driscoll on www.math.udel.edu/~driscoll/SC.

The results are shown in figure 11. Ignoring the wrong boundary geometry yields highly oscillating, completely useless solutions, regardless of the conductivity transformation used (a)–(c). In contrast, considering the boundary geometry by simultaneously estimating a conformally equivalent electrode configuration results in smooth conductivity estimations, which resemble the interior geometry of the true conductivity distribution (d)–(f). The best result is achieved when using the conductivity transformation $t_{\sigma\rho}$.

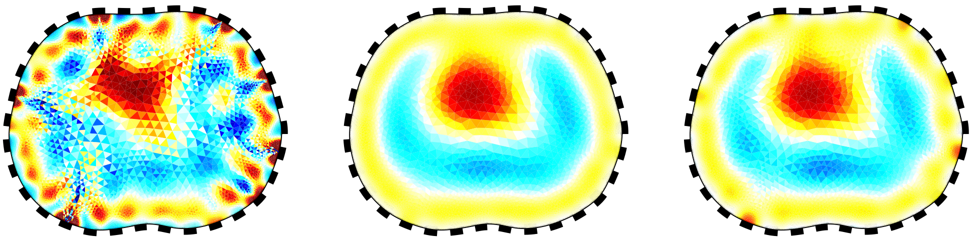

(a) Using F, t_{Id}: $k_* = 36, e_{\mathrm{rel}} = 41.43\%$.

(b) $\overline{F}$, t_{Id}, $t_{z,\log}$: $k_* = 16, e_{\mathrm{rel}} = 14.41\%$.

(c) $\overline{F}$, t_{Id}, $t_{z,\tan}$: $k_* = 13, e_{\mathrm{rel}} = 14.96\%$.

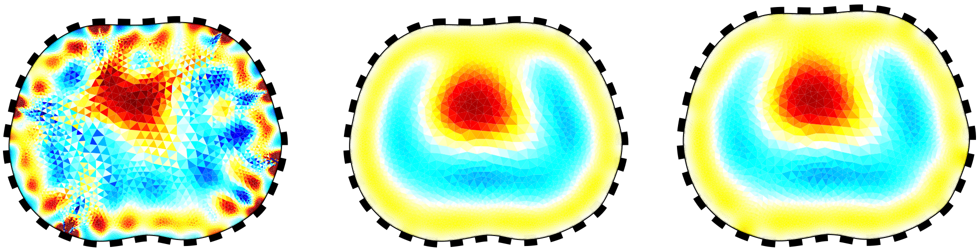

(d) F, $t_{\log}$: $k \ = 24, e_{\mathrm{rel}} = 43.16\%$.

(e) $\overline{F}$, $t_{\log}$, $t_{z,\log}$: $k \ = 22, e_{\mathrm{rel}} = 14.54\%$.

(f) $\overline{F}$, $t_{\log}$, $t_{z,\tan}$: $k \ = 17, e_{\mathrm{rel}} = 14.36\%$.

Figure 9. Reconstructions in the presence of unknown fluctuating contact impedances, analogous to figure 7. (a) Using F, t_{Id}: $k_* = 36, e_{\mathrm{rel}} = 41.43\%$. (b) $\overline{F}$, t_{Id}, $t_{z,\log}$: $k_* = 16, e_{\mathrm{rel}} = 14.41\%$. (c) $\overline{F}$, t_{Id}, $t_{z,\tan}$: $k_* = 13, e_{\mathrm{rel}} = 14.96\%$. (d) F, $t_{\log}$: $k_* = 24, e_{\mathrm{rel}} = 43.16\%$. (e) $\overline{F}$, $t_{\log}$, $t_{z,\log}$: $k_* = 22, e_{\mathrm{rel}} = 14.54\%$. (f) $\overline{F}$, $t_{\log}$, $t_{z,\tan}$: $k_* = 17, e_{\mathrm{rel}} = 14.36\%$.

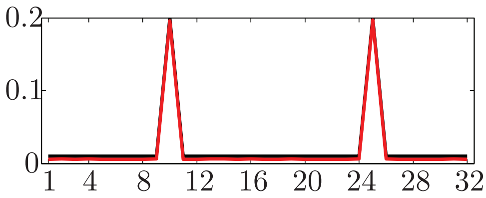

Figure 10. Exact (black) and recovered (red) contact impedances at the 32 electrodes setting considered in section 4.4.

4.6. Wrong contact impedances and wrong boundary geometry

Finally, we consider the thorax setting with both unknown boundary shape and unknown contact impedances. The ICP is now solved using the extended forward operator including the estimation of contact impedances, electrode positions and sizes simultaneously using the transformations $t_{\sigma\rho}$, $t_{z,\tan}$, $t_{\theta,\tan}$ and $t_{\omega,\tan}$, respectively.

The result is shown in figure 12 and compared to the solution of the untransformed conductivity estimation with fixed boundary parameters. In figure 12(b), we observe that the resulting conductivity estimate succeeds and is visually similar to the reconstruction of figure 6 with accurately known boundary configuration. Moreover, the relative estimation error is also on the same level. For reference, using $t_{\log}$ in the otherwise identical extended forward operator yields slightly worse results ($k_* = 72$, $e_{\mathrm{rel}} = 17.97\%$).

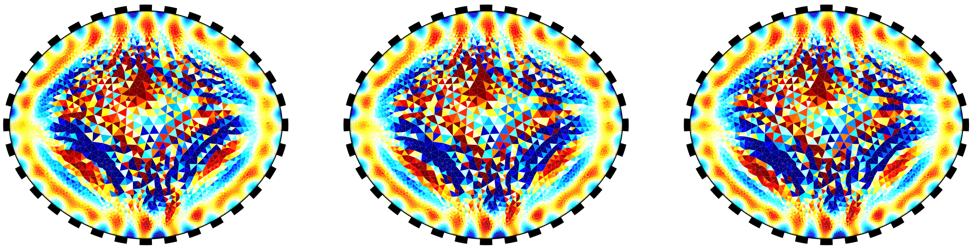

(a) Using F, t_{Id}: $k_* = 37, e_{\mathrm{rel}} = 58.03\%$.

(b) F, $t_{\log}$: $k_* = 34, e_{\mathrm{rel}} = 48.63\%$.

(c) F, $t_{\sigma\rho}$: $k_* = 34, e_{\mathrm{rel}} = 45.21\%$.

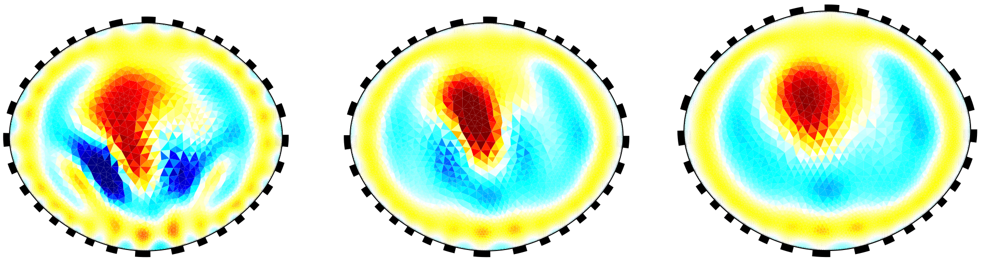

(d) $\overline{F}$, t_{Id}, $t_{\theta,\tan}$, $t_{\omega,\tan}$: $k_* = 69, e_{\mathrm{rel}} = 24.21\%$.

(e) $\overline{F}$, $t_{\log}$, $t_{\theta,\tan}$, $t_{\omega,\tan}$: $k_* = 73, e_{\mathrm{rel}} = 17.07\%$.

(f) $\overline{F}$, $t_{\sigma\rho}$, $t_{\theta,\tan}$, $t_{\omega,\tan}$: $k_* = 73, e_{\mathrm{rel}} = 14.52\%$.

Figure 11. Reconstructions of the thorax data on an elliptically shaped domain. Top row: only conductivity is estimated. Bottom row: conductivity and (transformed) electrode positions and sizes are estimated simultaneously. (a) Using F, t_{Id}: $k_* = 37, e_{\mathrm{rel}} = 58.03\%$. (b) F, $t_{\log}$: $k_* = 34, e_{\mathrm{rel}} = 48.63\%$. (c) F, $t_{\sigma\rho}$: $k_* = 34, e_{\mathrm{rel}} = 45.21\%$. (d) $\overline{F}$, t_{Id}, $t_{\theta,\tan}$, $t_{\omega,\tan}$: $k_* = 69, e_{\mathrm{rel}} = 24.21\%$. (e) $\overline{F}$, $t_{\log}$, $t_{\theta,\tan}$, $t_{\omega,\tan}$: $k_* = 73, e_{\mathrm{rel}} = 17.07\%$. (f) $\overline{F}$, $t_{\sigma\rho}$, $t_{\theta,\tan}$, $t_{\omega,\tan}$: $k_* = 73, e_{\mathrm{rel}} = 14.52\%$.

(a) Using F, t_{Id}: $k_* = 40, e_{\mathrm{rel}} = 71.92\%$

(b) $\overline{F}$, $t_{\sigma\rho}$, $t_{z,\tan}$, $t_{\theta,\tan}$ and $t_{\omega,\tan}$: $k_* = 65, e_{\mathrm{rel}} = 14.28\%$.

Figure 12. Reconstructions of the thorax setting for inaccurate boundary shape and unknown, fluctuating contact impedances, (a) using the untransformed forward operator F and (b) using the transformed extended forward operator $\overline{F}$. (a) Using F, t_{Id}: $k_* = 40, e_{\mathrm{rel}} = 71.92\%$. (b) $\overline{F}$, $t_{\sigma\rho}$, $t_{z,\tan}$, $t_{\theta,\tan}$ and $t_{\omega,\tan}$: $k_* = 65, e_{\mathrm{rel}} = 14.28\%$.

Further reconstructions, including some based on data from measured tank experiments, are presented in [23].

4.7. Reconstructions using untransformed boundary parametrizations

We have studied in section 3 how electrode parameter transformations do not only lift the constrainedness, but also can reduce nonlinearity and 'over-shooting' of parameter-updates

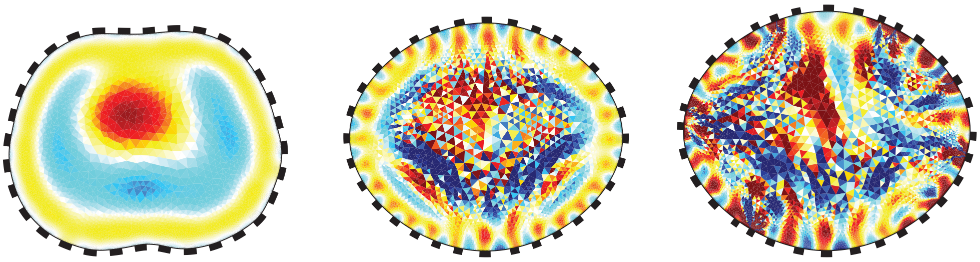

$\overline{F}$, t_{Id}, $t_{z,\mathrm{Id}}$:
$k_* = 72, e_{\mathrm{rel}} = 15.69\%$.

$\overline{F}$, t_{Id}, $t_{\theta,\mathrm{Id}}$, $t_{\omega,\mathrm{Id}}$:
$k_* = 84, e_{\mathrm{rel}} = 45.43\%$.

$\overline{F}$, $t_{\sigma\rho}$, $t_{z,\mathrm{Id}}$, $t_{\theta,\mathrm{Id}}$, $t_{\omega,\mathrm{Id}}$:
$k_* = 156, e_{\mathrm{rel}} = 168.6\%$

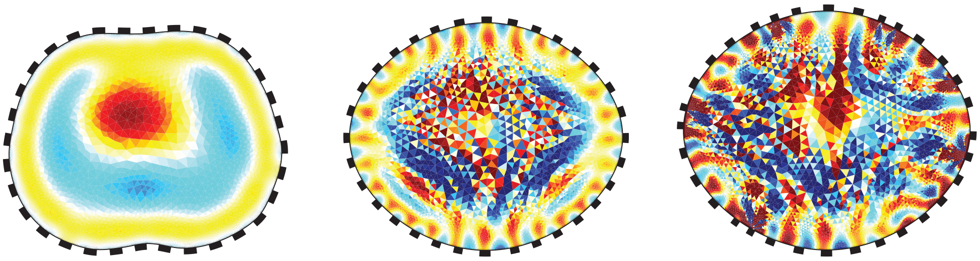

$\overline{F}$, $t_{\sigma\rho}$, $t_{z,\mathrm{Id}}$:
$k_* = 73, e_{\mathrm{rel}} = 15.75\%$,
Setting of section 4.4.

$\overline{F}$, $t_{\sigma\rho}$, $t_{\theta,\mathrm{Id}}$, $t_{\omega,\mathrm{Id}}$:
$k_* = 77, e_{\mathrm{rel}} = 41.24\%$,
Setting of section 4.5.

$\overline{F}$, $t_{\sigma\rho}$, $t_{z,\mathrm{Id}}$, $t_{\theta,\mathrm{Id}}$, $t_{\omega,\mathrm{Id}}$:
$k_* = 160, e_{\mathrm{rel}} = 193.0\%$,
Setting of section 4.6.

Figure 13. Reconstructions of the thorax data when omitting electrode parameter transformations. Top row: without conductivity transformation. Bottom row: with conductivity transformation.

due to linearization errors. For reference, the following reconstruction were performed using the extended forward operator with untransformed electrode parametrization. To avoid illegal electrode configurations, the updated electrode positions and sizes were projected back to an admissible configuration using the boundaries depicted in figure 2, while the contact impedances were, as implicitly done before, clamped to the interval $[10^{-4}, 10^{+4}]$. To distinguish between the impact of the interior and boundary transformation, both transformed and untransformed conductivity reconstruction is shown in figure 13.

Although the reconstruction of the untransformed contact impedances for known boundary configuration succeeds (with more iterations), the reconstruction of the untransformed electrode geometry fails. The author observed that during the iterations, some electrode positions and sizes tended to 'oscillate'. Moreover, some contact impedances had negative Newton updates (before clamping) even at the lower contact impedance limit, which would it make difficult to apply simple, commonly used line search strategies.

5. Summary and conclusion

We presented an extended, transformed forward operator for the ICP in section 2 which makes use of the Fréchet-differentiability with respect to the boundary configuration and implicitly ensures the admissibility of the configuration after Newton updates. For that reason, it can be conveniently integrated it into established Newton-type solvers for the ICP, like CG-REGINN, without setting-specific parameter tuning or line-search heuristics.

Moreover, we have motivated the theoretical advantage in terms of reduced nonlinearity when using favourable transformations in section 3 by investigating simple settings for which semi-analytic solutions are available.

Based on the numerical results in section 4, we conclude that the estimation of the conductivity succeeds in case of inaccurately boundary shape and unknown contact impedances when using the proposed extended and transformed forward operator $\overline{F}$ in the inexact Newton scheme CG-REGINN within the MANTIS reconstruction framework. In particular, the proposed solution can handle measurements with badly attached electrodes, fluctuating contact impedances, inaccurately known boundary geometry. These solutions are on par with the solution for perfectly known boundary geometry both visually and in terms of the relative reconstruction error.

Acknowledgments

The author would like to thank Andreas Rieder for valuable insights on inverse problems and their application to EIT as well as thoughtful suggestions and feedback regarding the content and presentation of this work. Moreover, the author is grateful to the two anonymous referees for careful review and valuable feedback, which helped to present the results more clearly.

ORCID iDs

Robert Winkler https://orcid.org/0000-0002-4493-6973

References

[1] Dardé J, Hyvönen N, Seppänen A and Staboulis S 2013 Simultaneous reconstruction of outer boundary shape and admittivity distribution in electrical impedance tomography *SIAM J. Imaging Sci.* **6** 176–98
[2] Dardé J, Hakula H, Hyvönen N, Staboulis S and Somersalo E 2012 Fine-tuning electrode information in electrical impedance tomography *Inverse Problems Imaging* **6** 399–421
[3] Vilhunen T, Kaipio J, Vauhkonen P, Savolainen T and Vauhkonen M 2002 Simultaneous reconstruction of electrode contact impedances and internal electrical properties: I. Theory *Meas. Sci. Technol.* **13** 1848–54
[4] Hyvönen N, Seppänen A and Staboulis S 2014 Optimizing electrode positions in electrical impedance tomography *SIAM J. Appl. Math.* **74** 1831–51
[5] Lechleiter A and Rieder A 2010 Towards a general convergence theory for inexact Newton regularizations *Numer. Math.* **114** 521–48
[6] Wahba G 1977 Practical approximate solutions to linear operator equations when the data are noisy *SIAM J. Numer. Anal.* **14** 651–67
[7] Hansen P 1992 Analysis of discrete ill-posed problems by means of the L-curve *SIAM Rev.* **34** 561–80
[8] Cheney M, Isaacson D, Newell J, Simske S and Goble J 1990 NOSER: an algorithm for solving the inverse conductivity problem *Int. J. Imaging Syst. Technol.* **2** 66–75
[9] Winkler R and Rieder A 2015 Model-aware Newton-type inversion scheme for electrical impedance tomography *Inverse Problems* **31** 045009
[10] Grychtol B and Adler A 2014 Choice of reconstructed tissue properties affects interpretation of lung EIT images *Physiol. Meas.* **35** 1035
[11] Barber D and Seagar A 1987 Fast reconstruction of resistance images *Clin. Phys. Physiol. Meas.* **8** 47

[12] Vauhkonen M 1997 Electrical impedance tomography and prior information *PhD Thesis* University of Kuopio

[13] Hyvönen N and Mustonen L 2018 Generalized linearization techniques in electrical impedance tomography *Numer. Math.* **140** 95–120

[14] Boyle A, Crabb M, Jehl M, Lionheart W and Adler A 2017 Methods for calculating the electrode position jacobian for impedance imaging *Physiol. Meas.* **38** 555

[15] Isaacson D 1986 Distinguishability of conductivities by electric current computed tomography *IEEE Trans. Med. Imaging* **5** 91–5

[16] Dobson D 1992 Estimates on resolution and stabilization for the linearized inverse conductivity problem *Inverse Problems* **8** 71–81

[17] Palamodov V 2002 Gabor analysis of the continuum model for impedance tomography *Ark. Mat.* **40** 169–87

[18] MacMillan H, Manteuffel T and McCormick S 2004 First-order system least squares and electrical impedance tomography *SIAM J. Numer. Anal.* **42** 461–83

[19] Borcea L, Druskin V, Guevara Vasquez F and Mamonov A 2011 Resistor network approaches to electrical impedance tomography *Inverse Problems and Applications: Inside Out* II vol 60 (Cambridge: Cambridge University Press) pp 55–118

[20] Winkler R and Rieder A 2014 Resolution-controlled conductivity discretization in electrical impedance tomography *SIAM J. Imaging Sci.* **7** 2048–77

[21] Cheng K, Isaacson D, Newell J and Gisser D 1989 Electrode models for electric current computed tomography *IEEE Trans. Biomed. Eng.* **36** 918–24

[22] Somersalo E, Cheney M and Isaacson D 1992 Existence and uniqueness for electrode models for electric current computed tomography *SIAM J. Appl. Math.* **52** 1023–40

[23] Winkler R 2016 A model-aware inexact Newton scheme for electrical impedance tomography *PhD Thesis* Karlsruher Institut für Technologie (KIT)

[24] Kaipio J, Kolehmainen V, Somersalo E and Vauhkonen M 2000 Statistical inversion and monte carlo sampling methods in electrical impedance tomography *Inverse Problems* **16** 1487

[25] Lechleiter A and Rieder A 2006 Newton regularizations for impedance tomography: a numerical study *Inverse Problems* **22** 1967–87

[26] Seagar A, Yeo T and Bates R 1984 Full-wave computed tomography. Part 2: resolution limits *IEE Proc. A* 131 616–22

[27] Demidenko E 2011 An analytic solution to the homogeneous EIT problem on the 2d disk and its application to estimation of electrode contact impedances *Physiol. Meas.* **32** 1453–71

[28] Winkler R, Staboulis S, Rieder A and Hyvönen N 2014 Fine-tuning of the complete electrode model *Proc. of the 15th Int. Conf. on Biomedical Applications of Electrical Impedance. Systems and Computer Engineering, Carleton University* p 28

[29] Hyvönen N, Majander H and Staboulis S 2017 Compensation for geometric modeling errors by positioning of electrodes in electrical impedance tomography *Inverse Problems* **33** 035006

[30] Rieder A 2005 Inexact Newton regularization using conjugate gradients as inner iteration *SIAM J. Numer. Anal.* **43** 604–22

[31] Isaacson D, Mueller J, Newell J and Siltanen S 2004 Reconstructions of chest phantoms by the D-bar method for electrical impedance tomography *IEEE Trans. Med. Imaging* **23** 821–8